

Article

Multispectral and Texture Feature Application in Image-Object Analysis of Summer Vegetation in Eastern Tajikistan Pamirs

Eric Ariel L. Salas *, Kenneth G. Boykin and Raul Valdez

Received: 26 August 2015; Accepted: 18 January 2016; Published: 21 January 2016

Academic Editors: Parth Sarathi Roy and Prasad S. Thenkabail

Department of Fish, Wildlife and Conservation Ecology, New Mexico State University, Las Cruces, NM 88003, USA; kboykin@nmsu.edu (K.G.B.); rvaldez@nmsu.edu (R.V.)

* Correspondence: easalas@nmsu.edu; Tel.: +1-575-646-2691

Abstract: We tested the Moment Distance Index (MDI) in combination with texture features for the summer vegetation mapping in the eastern Pamir Mountains, Tajikistan using the 2014 Landsat OLI (Operational Land Imager) image. The five major classes identified were sparse vegetation, medium-dense vegetation, dense vegetation, barren land, and water bodies. By utilizing object features in a random forest (RF) classifier, the overall classification accuracy of the land cover maps were 92% using a set of variables including texture features and MDI, and 84% using a set of variables including texture but without MDI. A decrease of the Kappa statistics, from 0.89 to 0.79, was observed when MDI was removed from the set of predictor variables. McNemar's test showed that the increase in the classification accuracy due to the addition of MDI was statistically significant ($p < 0.05$). The proposed method provides an effective way of discriminating sparse vegetation from barren land in an arid environment, such as the Pamir Mountains.

Keywords: object-based analysis; Pamir Mountains Tajikistan; Moment Distance; MDI; Marco Polo argali; multispectral application; image texture; arid environment

1. Introduction

Various remote sensing approaches have been devised to generate land-use/land-cover (LULC) maps with improved classification accuracy and with a relatively low production cost. Efforts to find crucial variables for classifying digital images and produce accurate LULC maps have been an important component of remote sensing studies in the past two decades [1,2]. Classification schemes that only utilize the spectral variables derived from image pixels used to be the most popular go-to procedure for LULC, delineating for instance, water bodies [3–5], urban areas [6–8], and vegetation [9,10]. In later research endeavors, apart from the spectral information, the spatial information or the relationship between neighboring pixels were explored through object-based image analysis (OBIA) [11,12]. The OBIA approach generally improves classification accuracy with respect to the traditional pixel-based approach [13–18]. OBIA is preferable since an object is represented in its true spatial landscape pattern instead of a squared classified pixel [19].

Texture variables have been widely used in OBIA and have been shown to improve discrimination and classification accuracy (e.g., [20–24]) in different land cover types. Texture measures the variability in habitat structure [25–27] using the distribution of grey levels among neighboring pixels in a digital image. It quantifies visual characteristics of the image, such as smoothness, roughness, symmetry, directionality [28], and the interactions of these characteristics [29]. Depending on the image source, texture can be calculated on single or multiple bands, with each yielding different information about the spatial relationships of neighboring pixels (*i.e.*, different categories of land cover and habitat

structure). Few studies (e.g., [30–32]) have used a single image spectral band that characterizes the spatial variability within the bands to compute texture images. However, being specific to only one band limits the texture information that a multispectral image may contain [33]. To avoid the need to choose a single band, a multiband texture could be derived from all appropriate spectral bands.

The combination of texture images plus a host of spectral data as input variables in the classification procedure provide reliable mapping results with high overall classification accuracies [34,35]. Nevertheless, to optimize the classification process, Stumpf and Kerle [36] suggest possible enhancements through the integration of other ancillary datasets or exploration of additional object metrics. There are a range of potentially useful object metrics for LULC mapping that have not been fully exploited. In this study, we explored the capability of the spectral metric Moment Distance Index (MDI) [37] as one of the predictor variables for landcover mapping in an arid environment.

The Moment Distance method exploits the available bands of the remote sensing image by analyzing the shape of the reflectance spectrum, and at each composite, calculating the moment distances among the bands in simple geometric operations (Section 3.4 explains more the method). By siphoning all the points of the reflectance curve, we can capture the diversity of the signatures of the landcover classes, especially for vegetation communities in an arid environment, as the MDI is unaffected by soil background and atmospheric effects [38]. Salas and Henebry [38] further illustrated the capability of the MDI to detect movements of the curve shape that may be caused by soil reflectance. The MDI also takes full advantage of the available information contained in a multispectral image, such as Landsat, by creating a new index that incorporates wavelengths not sampled by any broadband system.

The utilization of a large number of texture and spectral predictor variables in the classification may lead to the problem of high data dimensionality [28,39]. This problem requires a highly suitable computational statistical algorithm. Non-parametric machine-learning algorithms have emerged that have the capability to depict complex interactions among variables. Random Forest (RF) [40] is one such algorithm that has been adopted in several mapping applications [36,41] because it can handle high dimensionality effectively and is computationally efficient in both training and classification [17]. RF has also demonstrated lower test errors than conventional decision trees [42].

The goal of this paper is to extract reliable summer vegetation cover information from Landsat image in eastern Tajikistan Pamirs through utilization of a range of predictor variables, such as texture and spectral data. Taking advantage of the capability of the OBIA approach, our specific objectives are two-fold: (1) to investigate the potential of the MDI to improve the vegetation mapping in an arid community; and (2) to identify the best combination of components for image classification using the most appropriate segmentation settings under the RF classifier. Finally, the information on the spatial extent of vegetation cover resulting from this study could improve rangeland management and enhance the current knowledge of vegetation communities in the Pamir region.

2. Study Area

Tajikistan, situated in southern central Asia and with a human population of seven million, is bordered by China in the east, Afghanistan in the south, Uzbekistan in the northwest and Kyrgyzstan in the north. More than 90% of the country is mountainous with several mountains exceeding 7000 m in the eastern portion of the country and form the Pamir massif.

The study area (Figure 1), which covers large parts of the summer pasture areas of the Jamoat Kona Kurghan, is located in the southeastern Pamir Mountains of Tajikistan in the Gorno-Badakhshan Autonomous Region, between latitudes 37°N and 38°N and longitudes 74°E and 75°E and covers an area of approximately 223,000 ha. The rocky mountainous terrain has an elevation of 3500 m to 5500 m above mean sea level (amsl). The study area roughly corresponds to the area of a wild ungulate hunting concession in which 45 hunting permits are issued yearly at a cost of \$40,000 per permit [43]. Wild ungulates include argali (*Ovis ammon*) and Asiatic ibex (*Capra sibirica*). Domestic angulates include sheep, goats, and yaks [44].

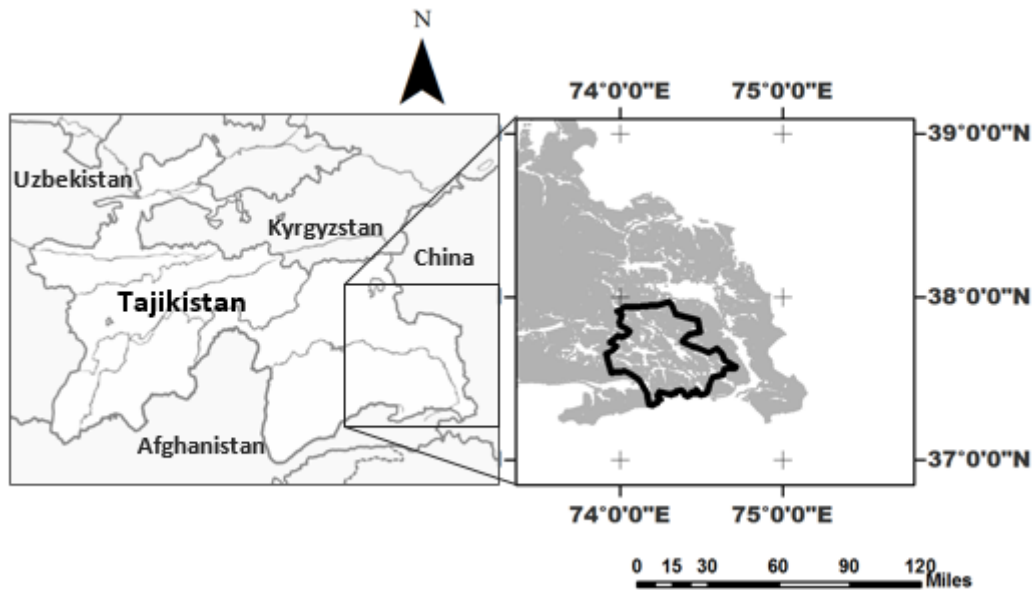


Figure 1. Location of the study area in the southeastern region of Tajikistan, based on a single Landsat 8 OLI scene from 15 July 2014.

Average annual precipitation is about 100 mm with subzero average temperatures from October to March. With such extreme climatic conditions, herding of yaks, sheep, and goats has been the primary agricultural option [45]. Domestic animals are transported to lower pastures during the fall, winter, and early spring (October–May) to avoid the harsh winter weather. The summer pastures are dominated by *Artemisia* and *Festuca* species, with productivity of 0.3 to 0.4 t·ha⁻¹ and 0.8 to 1.2 t·ha⁻¹, respectively [46]. Dominant vegetation plant forms are semishrubs including teresken (*Krascheninnikovia ceratoides*) and sagebrush (*Artemisia*), and several species of grasses, sedges, and forbs. Grazing competition between wild ungulates and livestock can occur on Pamir rangelands near human settlements [47,48].

3. Datasets and Methods

3.1. Field Data and Class Selection

We selected these main classes: vegetation, water, and barren land. Water class includes rivers and streams. Note that the rivers and streams may refer to riparian areas, which may not have flowing water throughout the year. We further subdivided the vegetation class based on [49] into “sparse vegetation,” “medium dense vegetation,” and “dense vegetation.” The motivation of the subdivision was the visually-observed density of plant communities during one of our summer vegetation surveys (Figure 2).

The fieldwork quantified species or genus composition, canopy coverage, and frequency of occurrence for plants. We refer the reader to Salas *et al.* [43] for additional details of the field data collection. Sparse vegetation on dry upland locations consisted mainly of *Poa* sp. and *Geranium* sp. Medium dense vegetation on dry meadow locations consisted mostly of *Blysmus compressus* sp. and *Rununculus* sp. Dense vegetation on wet meadows consisted mostly of *Carex* sp. and *Teraxacum* sp. These subdivision allowed us to focus in the identification of vegetation communities in the area. In addition, this also eliminated the problem of separability of vegetation classes when analyzing their reflectance responses from the satellite image.

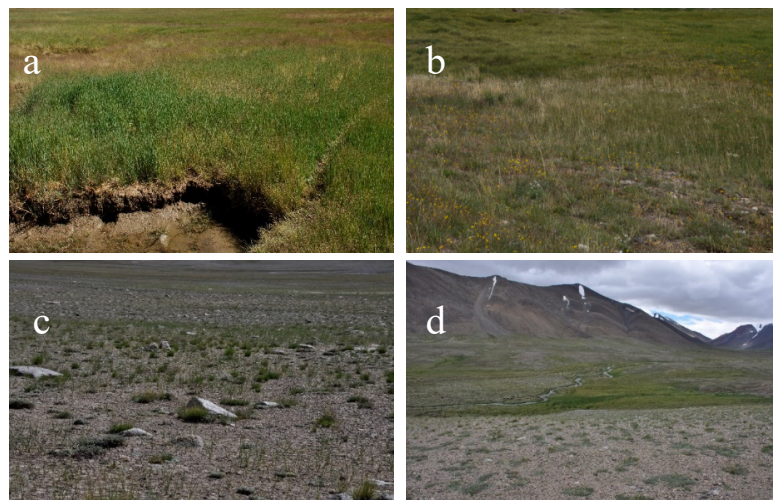


Figure 2. Summer fieldwork involved geotagging of vegetation communities based on three classes: (a) dense; (b) medium dense; and (c) sparse. The sample photo in (d) shows the transition between different classes. Geotagged locations are essential for classification and accuracy assessment.

3.2. Landsat Data

We used the level-1 terrain-corrected product (L1T) Landsat 8 OLI data from 15 July 2014 (path/row: 150/34) obtained from the U.S. Geological Survey Earth Resources Observation and Science (USGS EROS) resource archive [50]. With a minimal cloud cover of 4%, the month of July is within the period identified to be the vegetation peak for pasture [51]; the period when vegetation growth produces the highest spectral signals. The 30-m resolution of the Landsat is suitable for mapping in regional scales [52], but could be challenging, especially in arid environments, such as the Pamirs. The vegetation cover in the eastern Pamirs generally covers patches big enough to be detected by the resolution of the Landsat. High-resolution sensors may not offer a better performance [53], are impractical to apply to the total study area due to their high cost, and require a longer period of data analysis than medium spatial resolution image data [54].

3.3. Image Preprocessing

Preprocessing of the image enhances the quality of the data and removes inherent noise that can have negative impacts on the classification and the scene-to-scene comparisons over time, such as change detection [55,56]. We normalized the image by converting the measured digital number (DN) values to top of atmosphere (TOA) reflectance. It is the most important step in producing vegetation ratio indices products, such as the Normalized Difference Vegetation Index (NDVI) [57].

Screening of cloud patches, cloud shadows, and mountaintop snow was performed to ensure that the image was devoid of obstructions that may result in false classification. In the case of the clouds, we did visual and/or spectral examinations of the image to assess for cloud presence and shadow contaminations, delineating them and masking them out from the analysis.

We created the Normalized Difference Snow Index (NDSI) [58] image to distinguish snow from other surrounding features. A threshold was applied to the NDSI to filter the non-snow features that may have been misclassified as snow by examining reflectance at other wavelengths. Further, we did extensive manual deleting of isolated snow artifacts especially in transition areas between snow and non-snow features located in steep slopes.

3.4. Predictor Variables

Table 1 lists the input variables used in this study. Apart from the spectral and texture images, we added topographic variables. Studies highlighted that adding digital elevation model (DEM),

NDVI, and Modified Soil-adjusted Vegetation Index (MSAVI) [59,60] could help improve classification results in terms of feature discrimination and accuracy of featured classes. Incorporating a topographic variable like the DEM, slope, and aspect did not only depict the distribution of terrain components that influence spectral response [61], but also it increased the classification accuracy of digital data [60,62]. The processed DEM was sourced from NASA’s Shuttle Radar Topography Mission (SRTM) digital elevation dataset that is available for download through the USGS website [63]. NDVI [57] exploits the strong differences in the red and NIR reflectances where contrast between vegetation and soil is maximal [38]. Sensitive to pixel-level changes in greenness, NDVI is calculated as the difference between the spectral reflectance measurements of the NIR and red bands divided by the sum of the same measurements. With desert soils characterizing much of the Eastern Pamirs, MSAVI was used in the classification for vegetation sensitivity and soil noise reduction [64]. The index automatically adjusts to the energy proportion “seen” by the sensor, while retaining the dynamic range of the NDVI [65]. For more information about MSAVI, we refer the reader back to Qi *et al.* [64]. Further, we added Landsat bands data space to further separate classes, e.g., vegetation surfaces from soil and rock [66,67].

Table 1. Input variables considered in the derivation of the object features.

No.	Variables	Data Sources
1	Normalized Difference Vegetation Index (NDVI)	Landsat 8
2	Digital Elevation Model (DEM)	Shuttle Radar Topography Mission (SRTM)
3	Modified Soil-adjusted Vegetation Index (MSAVI)	Landsat 8
4	Band 2 Blue (480 nm)	Landsat 8
5	Band 3 Green (560 nm)	Landsat 8
6	Band 4 Red (660 nm)	Landsat 8
7	Band 5 NIR (870 nm)	Landsat 8
8	Band 6 SWIR 1 (1610 nm)	Landsat 8
9	Band 7 SWIR 2 (2200 nm)	Landsat 8
10	Slope	DEM
11	Aspect	DEM
12	MDI	Landsat 8

Texture images can be derived from either of two measures—occurrence or co-occurrence. Occurrence measures use the number of occurrences of gray level with the processing window for texture calculations and are not as effective as co-occurrence measures which use the relative frequencies between two pixel brightness values linked by spatial relation [68,69]. Therefore, we utilized the co-occurrence measures that use a matrix to calculate the texture values within the processing window. This gray-level spatial dependence matrix [70] is a function of both the angular relationship and distance between two neighboring pixels. Various studies (e.g., [71–73]) have found the co-occurrence measure useful for LULC classification. We used the following eight textural features: homogeneity (HOM), second moment (M2), dissimilarity (DIS), entropy (ENT), contrast (CON), mean (MEA), variance (VAR), and correlation (COR). The software ENVI supports these textural filters [74] that are based on co-occurrence measures. The eight texture features were computed from each Landsat band (Table 1).

The Moment Distance (Figure 3) [37] is an analytical framework that focuses on the curve structure and detects the shape of the reflectance curve. The robustness of the method in defining the curve derives from the refereed distances from two point locations designated as shorter and longer pivot wavelength region (PWR). Assume that a reflectance curve is displayed in Cartesian coordinates with the abscissa displaying the wavelength λ and the ordinate displaying the reflectance ρ . The subscript LP denotes the *left pivot* (located in a shorter wavelength) and subscript RP denotes the *right pivot* (located in a longer wavelength). The λ_{LP} and λ_{RP} are the wavelength locations observed at the left and right pivots, respectively, where left (right) indicates a shorter (longer) wavelength.

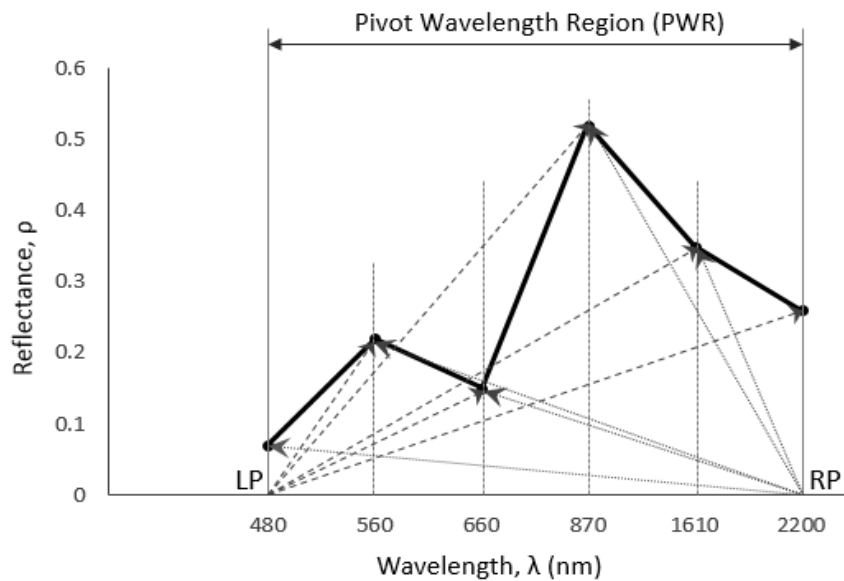


Figure 3. Schematic diagram of MDI applied on a sample spectral reflectance curve of a green vegetation. Note that the number of points between LP and RP pivots can vary depending on the number of bands analyzed or the width of the pivot wavelength region.

The moment distance from the left pivot (MD_{LP}) is the sum of the hypotenuses constructed from the left pivot to the value at successively longer wavelengths (index i from λ_{LP} to λ_{RP}); one base of the triangle is the difference from the left pivot ($i - \lambda_{LP}$) along the abscissa and the other is simply the value at i (Equation (1)). Similarly, the moment distance from the right pivot (MD_{RP}) is the sum of the hypotenuses constructed from the right pivot to the value at successively shorter wavelengths (index i from λ_{RP} to λ_{LP}); one base of the triangle is the difference from the left pivot ($\lambda_{RP} - i$) along the abscissa and the other is the value at i (Equation (2)). Although the MDI produces a single value for every PWR, it is an unbounded metric (Equation (3)). Being variable, it increases or decreases as a nontrivial function of the number of spectral bands considered and the shape of the spectrum that spans those bands. As the MDI is designed to exploit the multiple band counts, the new metric may lose its capability to detect shape changes of the curve when applied to very few bands.

$$MD_{LP} = \sum_{i=\lambda_{LP}}^{\lambda_{RP}} \sqrt{\rho_i^2 + (i - \lambda_{LP})^2} \quad (1)$$

$$MD_{RP} = \sum_{i=\lambda_{RP}}^{\lambda_{LP}} \sqrt{\rho_i^2 + (\lambda_{RP} - i)^2} \quad (2)$$

$$MDI = MD_{RP} - MD_{LP} \quad (3)$$

Figure 4 demonstrates the changes of the MDI values when applied to reflectance curves from Landsat OLI bands. A curve with a well-defined peak (Figure 4a) will differ from a less-defined peak curve (Figure 4c) when defined by moment distances with varying pivot ranges. In Figure 1a, for instance, by fixing the LP and increasing the PWR one band at a time (going from reference point 2 to point 1), a slope becomes evident (e.g., sudden increase of MDI) when the NIR reflectance is contained within the pivot range. The rise of MDI around bands 4 and 5 defines the largest difference of the change of shape detected by a particular pivot pair. A similar pattern is observed when fixing the RP and increasing the PWR one band at a time (going from reference point 1 to 2).

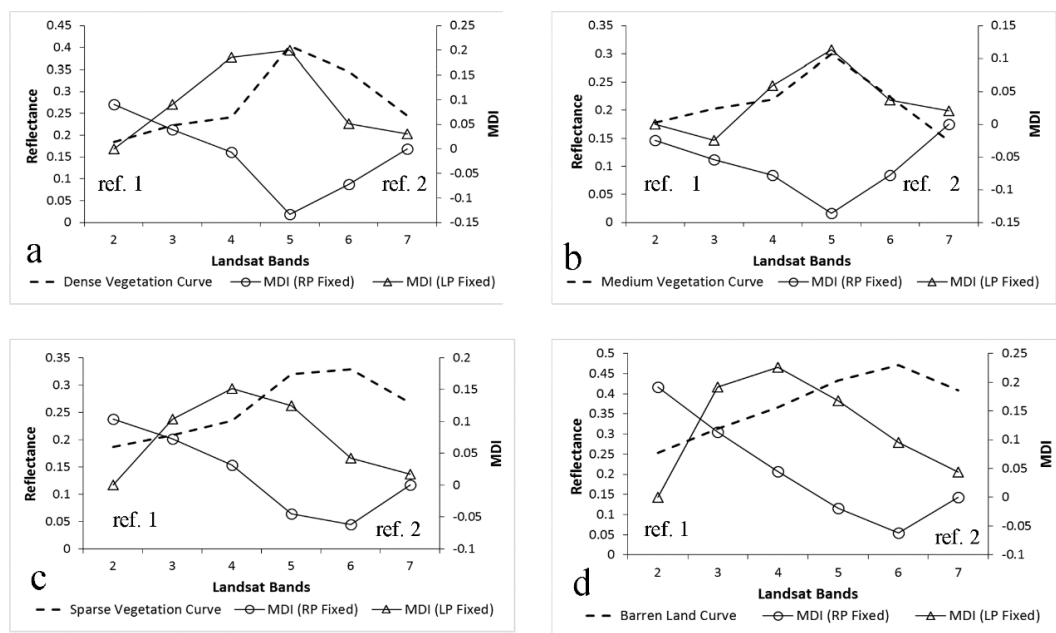


Figure 4. Sample illustrations of MDI applied to the reflectance responses of: (a) dense vegetation; (b) medium dense vegetation; (c) sparse vegetation; and (d) barren land, derived from the Landsat OLI image. The figures demonstrate the changes of the MDI values with varying PWR, moving from reference point 1 to 2, and *vice versa*. Maximum values are observed at maximum shape differences, usually occurring at the inclusion of a spectral curve peak or a spectral curve dip.

In Figure 4a,b, the reflectance curves of dense and medium dense vegetation classes are similar visually. However, MDI defines the two curves differently when considering the LP and RP. Medium dense vegetation exhibits more negative MDIs than dense vegetation, which causes the MDI (RP Fixed) to have a much broader curve opening (Figure 4b, between bands 4 and 6). The reflectance curves of sparse and barren land can also be confused (Figure 4c,d). However, MDI detects the minimal differences of the shapes of the two curves. In Figure 4c, MDI (RP fixed) has a slight upward bend when it moves from band 2 to band 5, which is caused by the presence of the dip of the reflectance between red and NIR. This bend is absent in Figure 4d, MDI (RP fixed).

With the Landsat, the use of the PWR from band 2 to band 7 encompasses the significant peak and/or dip of the reflectance curve that could lead to the shape difference maxima: the maximum difference of the summation of distances from point 1 (Equation (1)) and the summation of distances from reference point 2 (Equation (2)). The value of the difference reflects how the shape of the reflectance curve as viewed from reference point 1 varies from the one viewed from reference point 2. Shape dissimilarities are detected by comparing MD behaviors from these two reference points. Detecting the differences in shape is a crucial step in discriminating between landcover classes during classification.

In this paper, we only utilized one PWR that covers band 2 (LP at 480 nm) to band 7 (RP at 2200 nm).

Finally, MDI uses both the reflectance value and the distance between bands to compute a distance matrix that is sensitive to the changes of the shape of the reflectance curve. The index is specifically sensitive in the VIS to NIR regions where there is a strong difference in the reflectances. Also, there is not a significant effect of soil reflectance on the MDI at the strip of curve in the red-edge region, a region between the red and NIR [38].

3.5. Image Segmentation

We tapped the capability of the ENVI 5.2 software to produce the image objects. The ENVI segmentation algorithm requires a scale level and an optimal window size to segment the image.

Picking a low scale level could result into over-segmentation, while choosing a high scale level could cause fewer defined segments [1]. For the purpose of evaluating the influence of scale to the segmentation process, we selected six scale levels (10, 20, 30, 40, 50, and 60), a similar approach used by Frohn *et al.* [75]. Image objects created at fine scales may represent small real-world objects or patches, while those at coarser image segmentation scales may provide information on larger real-world objects like denser vegetation. For the optimal window size, we examined the spatial correlation between pixels in close proximity. We employed the variogram and correlogram statistical methods to find the highest variance/correlation derived from the smallest window size. The lag distance, in pixels, at which the variogram or the correlogram starts to flatten is the window size of interest. To capture vegetation communities, the window size for our analysis was set to 5 pixels or 5×5 as shown in the averaged correlogram and semivariogram plots from the bands of the Landsat image (Figure 5). Rodriguez-Galiano *et al.* [28] found the same window size to be important when mapping land cover using Landsat TM image. Further, a medium size window (5×5) was the best size to express desert variability after radiometrically calibrating multi-spectral imaging sensors [76], and to classify broad classes such as grass and bare land [77].

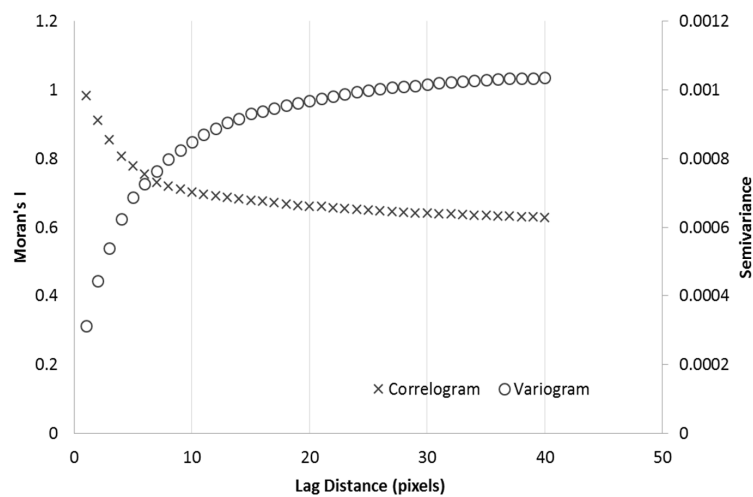


Figure 5. Averaged correlogram and semivariogram plots from the six bands of the 2014 Landsat image, showing the optimal lag distance (~5 pixels) with the highest variance.

Together with the input variables in Table 2, the texture images computed from each Landsat band, and each object metric evaluated in six different scales, a total of 312 variables were calculated from the satellite imagery. The addition of another window size would considerably multiply the number of input variables, which is already high for a single window analysis.

Table 2. Estimates of landcover classes (ha) considered in the analysis in the study area. Set 1 uses a set of variables that include texture features and MDI, and Set 2 uses a set of variables that include texture features but without MDI.

Class	Set 1 (with MDI)		Set 2 (without MDI)	
	Area (ha)	Share (%)	Area (ha)	Share (%)
Dense Vegetation	3902.03	1.62	2697.12	1.12
Medium Dense Vegetation	11676.41	4.86	6633.74	2.76
Sparse Vegetation	20121.37	8.37	9452.93	3.93
Barren Land	204208.17	84.96	220951.70	91.93
Water Bodies	446.11	0.19	618.60	0.26
Total	240354.09	100.00	240354.09	100.00

3.6. Random Forest Classifier

All resulting object-based data were imported into Random Forest. It is a supervised classification that uses nodes to create decision trees as base classifiers. It partitions high-dimensionality data into classes of interest. Using out-of-bag (OOB) sampling, it gives a measure of the internal cross-validation accuracy. RF is a convenient method for LULC mapping as it does not require assumption of the underlying distributions of the dataset input [78]. Homer *et al.* [79] showed the importance of a decision tree method when used to derive the National Land Cover Dataset (NLCD) using Landsat.

Apart from RF being robust for high-dimensionality data even if the data is noisy [80], the algorithm is also capable of measuring the importance of the individual input variables in the classification. This enhances the use of the RF classifier as a tool to combine with OBIA. We used the tool called *imageRF* [81] that can be implemented in an IDL/ENVI environment for the classification of remote sensing images with RF. We fixed the number of decision trees at 1000 to minimize the generalization error [36,82], and just enough not to increase the computational time [34].

To assess the importance of MDI to the classification, we ran RF using all 312 input variables (Set 1) and then reran the RF classifier without the MDI (Set 2), producing two classified maps.

3.7. Classification Assessment

The training samples were carefully chosen with the aid of Google Earth engine, authors' expert knowledge of the area, and the spectral signatures of the classes. Sixty ground reference points that were obtained in a field survey during the same summer month the Landsat image 2014 was taken and another 21 points obtained in July 2015, plus high resolution images of QuickBird (60-cm resolution) and WorldView-2 (50-cm resolution) that covered portions of the study area from 2003 to 2013, were both helpful in making decisions for class assignment. A total of 571 sample points were collected—140 samples for each of the vegetation class, 100 for barren land, and the rest is for water bodies. The *imageRF* tool randomly divided the samples into two sets: for training (70%) and for validation (30%).

Map classification accuracies were assessed using overall accuracy (OA), producer's accuracy (PA), user's accuracy (UA), and kappa coefficient. PA quantifies the error of omission, while UA quantifies error of commission. Kappa is the measure of agreement or accuracy of the classification [83]. It is more robust than OA as it takes into account the agreement occurring by chance [84]. Confusion matrices were constructed to assess the result of each image classification (e.g., [85,86]), to provide an indication of the classification agreement between two maps (the classified *vs.* referenced maps) that is not attributable to chance.

Finally, we performed McNemar's parametric test to quantify the statistical significance of the difference between the two classification results. The test is based on a chi-square statistics, computed from two error matrices.

4. Results

Figure 6 lists the top 50 object features according to their importance in the RF model. A high value of the normalized variable (which was based on the accuracies of the permuted out-of-bag samples, accuracies of the original samples, and the standard deviation) indicates that the variable has a high contribution for the entire RF. The input layers at the top of the list were predominantly based on spectral data, such as NDVI and MDI, with the exemption of the DEM that ranked within the top three. While multispectral information dominated the top 10, object features based on texture were located in the next 10. Dissimilarity, homogeneity, contrast, and second moment led the list of importance for texture measures. Other texture measures, such as variance, entropy, correlation, and mean, were ranked relatively lower. Topographic variables slope and aspect were both absent in the top 50.

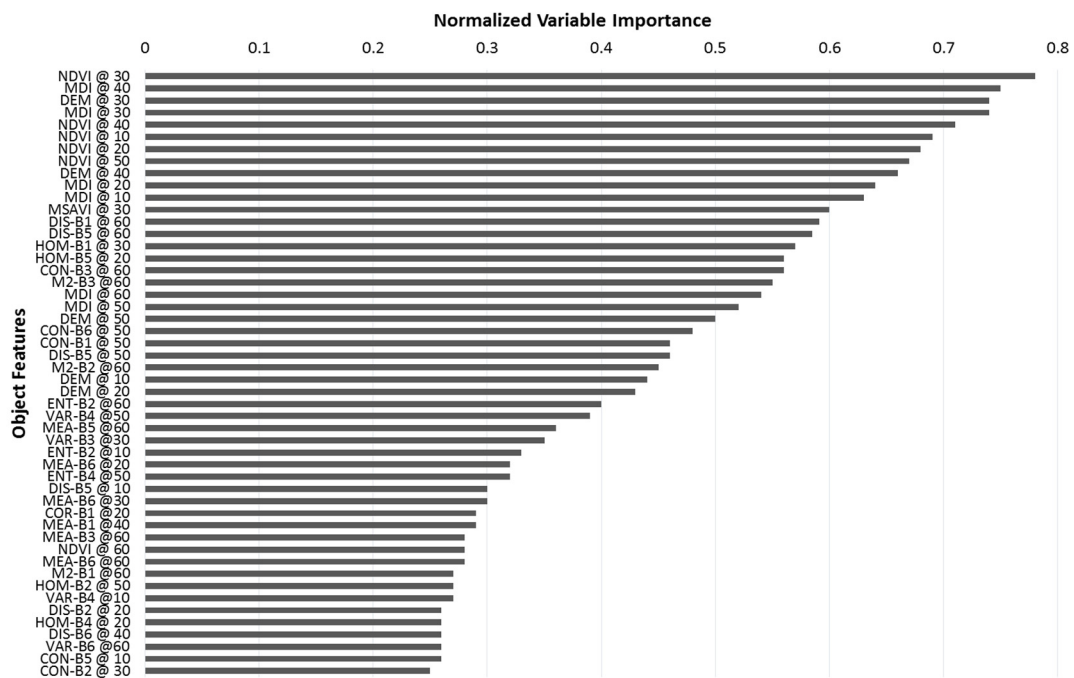


Figure 6. Rankings of the 50 most important object features in the RF model. Variables with high Normalized Variable Importance values, such as NDVI and MDI, are deemed highly important in the classification. The scales are also listed after the “@” symbol. HOM = homogeneity, CON = contrast, M2 = second moment, ENT = entropy, VAR = variance, MEA = mean, DIS = dissimilarity, COR = correlation, DEM = Digital Elevation Model. B2 to B7 are Landsat OLI bands 2 to 7.

Scalewise, medium coarse image segmentation scales (30 and 40) dominated the top 5. Finer scales (10 and 20) of the NDVI and MDI were in the next 5. Much coarser scales (50 and 60) constituted the top list of the top-ranking texture measures. Considering all input variables, the medium coarse image segmentation scales for variance, entropy, correlation, and mean measures were listed at the very end. The MDI segmented at the scales of 50 and 60 ranked below the top-ranking texture features.

Band 2 (Blue, 450–510 nm), band 4 (Red, 640–670 nm), and band 6 (SWIR 1, 1570–1650 nm) were the most important Landsat bands in the RF model, but only when in combination with the top-ranking texture measures. Bands 5 (NIR, 850–880 nm) and 7 (SWIR 2, 2110–2290 nm) were present mostly between the 25th and 50th rankings.

MSAVI, the vegetation index designed to address the limitations of NDVI caused by soil background interference, ranked in the top 20. However, only the scale at 30 was present in the top 50, the rest of the scales appeared in the bottom of the list.

The areal estimates of the landcover classes are shown in Table 2. In Set 1 (with MDI), about 204,208 ha was covered by barren land, while a much bigger area of barren land (220,952 ha) was covered in Set 2. Dense vegetation for Set 1 has a 1.62% share (3902 ha), compared to 1.12% for Set 2 (2697 ha). Among all classes, sparse vegetation showed the most differences in area classified, a little over 20,000 ha for Set 1 and less than 10,000 ha for Set 2. The differences are reflected in the loss of sparse vegetation patches (Figure 7 Set 2 *vs.* Figure 7 Set 1), especially in the northern part.

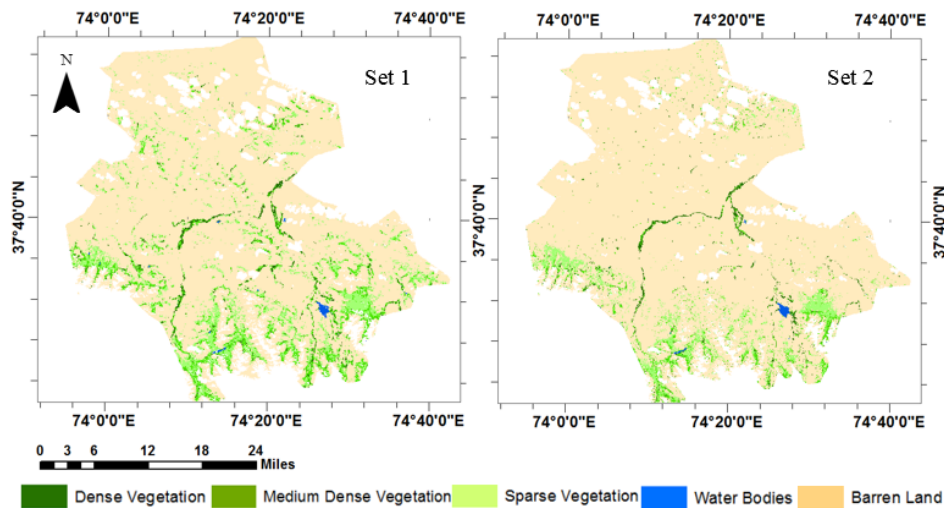


Figure 7. Map classifications showing the five landcover classes. Set 1 uses all object features with MDI, while Set 2 uses all object features without MDI.

About 71% of the dense vegetation for Set 1 and 56% for Set 2 was within two miles from rivers and streams (Figure 8). Seventy-six percent of sparse vegetation was between two miles and eight miles from the rivers or streams for Set 1 and 86% for Set 2. High percentage of vegetation coverage (90%) was observed at high mountain altitudes, at 4600 m amsl and below. Sparse vegetation located at much lower elevations of 4200 m amsl, specifically at the northeastern region, was poorly detected by Set 2 variables (Figure 8).

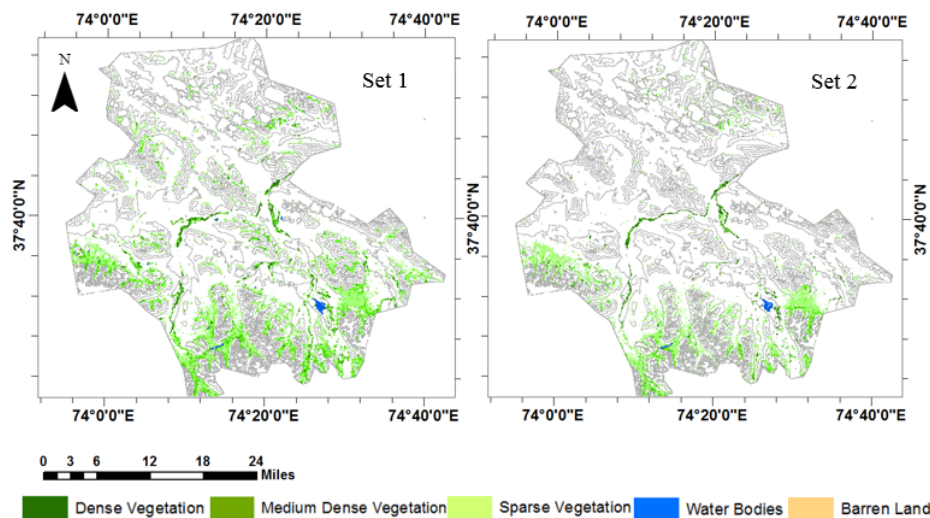


Figure 8. Map of the spatial distribution of the vegetation classes relative to the rivers/streams and the elevation layers. Note that dense vegetation is mostly found near rivers and water bodies.

The classified maps indicated an overall accuracy of 92% and 84% for Set 1 and Set 2, respectively (Table 3). Dense vegetation achieved high level of user's accuracy with 95% and 91%, respectively for Set 1 and Set 2. There was more confusion between sparse vegetation and barren land in Set 2 than in Set 1. The overall kappa statistics for the two maps were 0.89 and 0.79. Set 1 variables produced a classification result that revealed good agreements between the references and the classified maps. Our improved mapping strategy produced a map with more than 85% of the pixels classified correctly with respect to what would be expected by random assignment, satisfying the minimum requirement by Anderson *et al.* [87].

The difference between the accuracy achieved by the two sets of variables, Set 1 *vs.* Set 2, was analyzed using McNemar's test. The test result was 7.41 (exceeding the 5% significance level, *i.e.*, $Z > 1.96$), which signifies that the accuracy increase shown in the classification with a set that included the MDI over a set of variables without MDI was statistically significant at the 5% level. The test showed significant improvement of the map derived from Set 1 over the map derived from Set 2.

Table 3. Summary of the classification accuracy (%) and Kappa statistics for Set 1 (with MDI) and Set 2 (without MDI) maps.

Set of Variables Class	Set 1 (with MDI)				Set 2 (without MDI)			
	PA (%)	UA (%)	OA (%)	Kappa Statistics	PA (%)	UA (%)	OA (%)	Kappa Statistics
2014 Landsat Image								
Dense Vegetation	95.9	94.7			93.4	91.2		
Medium Dense Vegetation	86.3	88.0			75.9	79.0		
Sparse Vegetation	83.2	89.0	92.1	0.89	68.5	76.0	84.0	0.79
Barren Land	95.8	91.3			86.9	79.3		
Water Bodies	100	100			96.1	100		

Apart from the initial tests that we performed to examine the responses of MDI at various reflectance curves (Figure 4), we further tested pixel-wise the response of MDI in varying percentages of the two main confusing classes: sparse vegetation and barren land. We chose 10 pairings (test samples) from sparse vegetation and barren land classes, satisfying the following criteria: (1) the pairs should be neighboring pixels; (2) both pixels were classified correctly in Set 1, but at least one pixel was misclassified due to confusion in Set 2; and (3) they must exhibit somewhat equal pixel values in Set 2 that resulted in misclassification. We linearly combined spectral curves of sparse vegetation and barren land to a specified mixture. For instance, a combination of 90% sparse vegetation and 10% barren land resulted in a curve that was dominated by sparse vegetation. These mixtures showed how MDI could enhance the distinction between sparse vegetation and barren land, even though these two classes share almost similar spectral properties and can be easily confused.

Differences of the shape of the spectral curves are shown in Figure 9a. In Figure 9b, decreasing values of the MDI were observed at increasing influence of the reflectance of the barren land. A high MDI value was related to a high percentage of sparse vegetation, while a low MDI value was related to a high percentage of barren land.

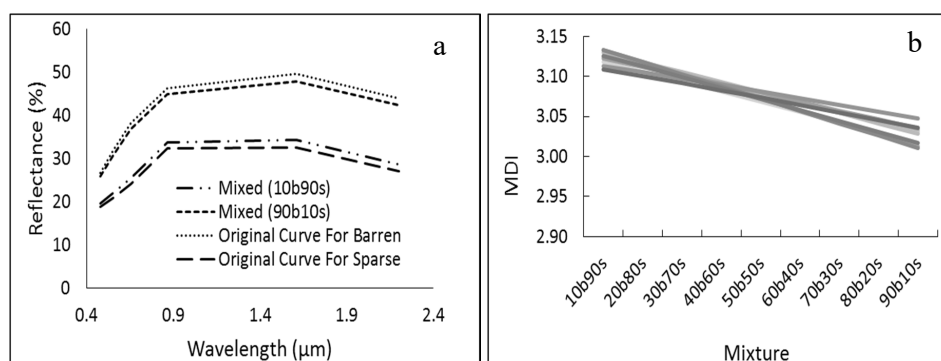


Figure 9. In (a), sample spectral curves of the barren land and sparse vegetation classes are shown with the original curve plus the curves with mixed reflectances. In (b) are values of the MDI at varying mixture of spectral reflectance. A mix of 90b10s indicates 90% barren land and 10% sparse vegetation, while a mix of 10b90s indicates 10% barren land and 90% sparse vegetation.

5. Discussion

The mapping of vegetation in the eastern Pamirs is basic for managing rangelands in this arid region. Although we employed a coarse mapping scheme by not taking into account vegetation species, the three vegetation groups selected in this study made delineation of classes more substantial as the scheme helped eliminate classification errors [88].

5.1. Classification Accuracy

Using the object features, the overall classification accuracy for Set 2 (with texture variables) was greater than 80%. This was comparable to Hergarten [20] that also used texture images to improve landuse classification. However, the other map produced by Set 1 (with texture and MDI as predictor variables) showed relatively few misclassification errors and an improved classification accuracy (>90%, kappa of 0.89). Zhang *et al.* [21] produced comparable accuracy results using a support vector machine (SVM), but with lower kappa statistics (kappa = 0.84).

The results for both sets indicated that the greatest amount of confusion, thus, poor discrimination, occurred between sparse vegetation and barren land classes, as well as between sparse vegetation and medium dense vegetation. The most probable explanation for this is that an area with a low vegetation cover could appear spectrally and texturally very similar to barren land. The same way applies for sparse vegetation and medium dense vegetation. However, Set 1 showed more promise of improved mapping analysis between these paired classes compared to Set 2 (Figure 10). Relative to dense vegetation with or without MDI, the PA and UA accuracies for both sets were comparable. This indicated that the combined spectral and texture variables were sufficient to map dense vegetation. Water bodies were identified more accurately than the rest of the classes.

The increases in the kappa coefficients between the two maps are statistically significant in terms of McNemar's test (at the 95% confidence level). The proposed use of object features in the RF classifier, exploiting the multivariate texture variables in conjunction with spectral derivatives (e.g., NDVI and MDI), offered an effective way of differentiating the landcover classes of an arid environment such as the Pamirs.

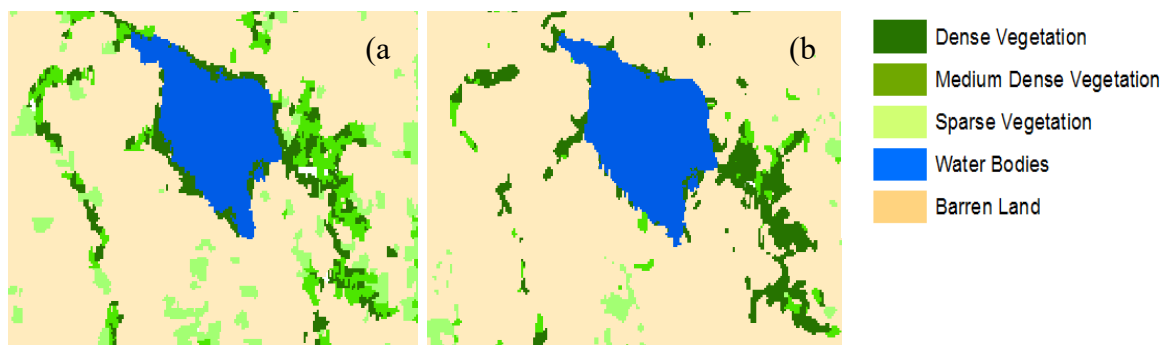


Figure 10. Classification results zoomed near a body of water. In Set 1 (a) with MDI, more patches of sparse vegetation exist compared to Set 2 (b) without MDI that classified the patches as barren land.

Our results indicated that Set 1 reduced the overall confusion between vegetation classes and barren land, which led to a much higher accuracy. The less robust discrimination between vegetation and the barren land in Set 2 may be attributed to the limitations in which reference samples were collected. We observed some test samples falling in patches of barren land surrounded by vegetation, which may eventually led to barren land misclassified as vegetation. These misclassification errors were explained by Maillard [89] as the edge effect of the texture property. Further, we observed problem areas between vegetation and water bodies especially with small patches of vegetation along river streams that led to confusion in Set 2. All in all, the misclassifications observed in Set 2 were reduced and less evident in Set 1.

5.2. Contribution of Predictor Variables

While we have shown that MDI improved the classification accuracy, no single object feature dominated the effectiveness of the vegetation mapping. When appropriate spectral indices, multivariate texture images, and a couple of topographic variables were combined in the RF classification algorithm, the landuse classes were more accurately extracted. The use of multivariate texture variables had shown to be an effective approach and that spectral information alone may not be sufficient for classifying Landsat object features in an arid environment.

5.2.1. Importance of Spectral Variables

We supposed that because the spectral response of vegetation in semiarid to arid environments tends to be affected by soil reflectance [64], the introduction of the MSAVI would be beneficial. Nevertheless, only one MSAVI object feature at scale 30 was present in the list of the top 50 important variables. This is in contrast with Laliberte *et al.* [90] that showed the index as having a high explanatory power when used for mapping arid rangelands.

Among all variables used in the classification, we expected NDVI to be the most important. The importance of NDVI was reflected in Figure 6, as all NDVI image objects from all scale levels can be found at the top of the list. Our results confirmed the NDVI input variable at all segmentation levels as the top object feature [82].

5.2.2. Importance of Topographic Variables

Slope had little to no contribution in the classification process. The inclusion of the DEM as one of the bands of the image has improved the classification results with higher accuracy [91] as shaded soil features were better discriminated against vegetation, especially those on the steep slopes [92]. We found that without DEM a number of dark bare land pixels along the steep slopes were misclassified as water pixels. DEM eliminated the classification problem by discriminating both classes.

5.2.3. Importance of Texture Features

Texture variables based on the gray level co-occurrence matrix also contributed to the increased accuracy in the classification. Texture allowed the extraction of image structures that are not detectable by spectral characteristics alone [43,49]. The use of all eight texture features (e.g., [21]) in the RF classification, may not be advisable for future studies. Results showed that only four texture features displayed superior worth in enhancing the classification. These four texture features—DIS, HOM, CON, and M2—had relatively high scores among all texture image objects especially in the coarser scales (50 and 60) (e.g., [90]). A coarser segmentation level permitted more pronounced disparities between neighboring pixels, which allowed more subtle distinctions between landcover classes. The pairings of these four texture features with red, IR, and blue bands (Figure 6) further vindicated their high ranks in the classification. The bands red, IR, and blue bands are useful for mapping soil and plants, even discriminating different types of plants [93]. Kraudzun *et al.* [94] also confirmed the importance of the blue band, specifically when used in OBIA. However, we caution the complete exclusion of the other bands. Bands 3, 5, and 7 were also in the top 50 and adding any one of the three bands in the classification may increase accuracy.

5.2.4. Importance of MDI

MDI showed the most potential among all variables. Exclusion of MDI considerably lowered the kappa from 0.89 to 0.79. Capturing additional information from the Landsat bands added value in studying the spectral behaviors of the classes that may not be possible for other indices. The advantage of the MDI against other metrics (e.g., [37,38]) is threefold. First, there is no requirement in the MDI to select the best bands in its equation as it utilizes the available bands of the Landsat product. Second, the moment distance algorithm characterizes the shape of the reflectance curve, such that a change of

the shape could mean distinction between classes. Third, MDI is unaffected by soil reflectance and may perform well in an arid environment. While there was more confusion in the separation between the sparse vegetation and barren land using the variables in Set 2, MDI facilitated in differentiating the two classes as reflected in Figure 10. MDI managed to discriminate the shapes of the reflectance curves (Figure 4) of the sparse vegetation and barren land, resulting in high values for areas dominated by sparse vegetation and low values for areas of barren land (Figure 9).

5.2.5. Importance of Scale

In terms of scale level, medium coarse image segmentation scales (30 and 40) were considered important. Object features from NDVI, MDI, and DEM using scales of 30 and 40 dominated the list of influential variables. Liu and Xia [95] showed the positive effect of medium coarse image segmentation scale to classification units. MDI at lower scale levels ranked below some of the texture variables such as DIS, HOM, M2, and CON.

In general, the integration of ancillary data as features for object-based classification confirmed previous applications [24,25] of satisfactorily discriminating land cover classes, with relatively better results than the Landsat spectral information alone. While having additional information to aid with classification is beneficial, it could also become increasingly challenging to identify variables that are most efficient for isolating the features of interest. The RF tool of identifying variables could help ease the challenge.

6. Conclusions

The use of the 30-m resolution Landsat images plus a variety of ancillary data satisfactorily classified the five landcover classes analyzed in this study. Although the decision to use a medium-coarse resolution image over a high-resolution one invites questions of its accuracy in mapping the vegetation in an arid region, our results at least supplement existing vegetation research in the eastern Pamir region.

The most important results of this study are shown in the high level of accuracy and kappa statistics we obtained when we applied texture object attributes (extracted from relevant Landsat bands) plus the MDI to RF classifier. Using the image segments within the RF has shown to be a great addition to tools for mapping analysts. Image segments added more information with respect to just considering individual pixels. The inclusion of texture images and the MDI variable in mapping the arid environment such as our study area has shown to significantly increase the mapping accuracy than just using spectral information.

The utilization of dissimilar but important components was pivotal in ensuring the methodology's good performance. The methodology we employed was designed to assimilate the spatial component of the landscape. Results confirmed the importance of using OBIA for landcover studies as the scale level can be adjusted for different land features. Our methodology would make it possible to (1) map the summer vegetation cover of the eastern Pamirs with much higher confidence; (2) find texture attributes for the image bands and combined it with MDI that enabled a better separation of vegetation and barren land classes; and (3) use for other landcover classifications in other regions of Tajikistan. Overall, our method and results not only provide a better understanding of the spatial distribution of the summer vegetation resources in the study area, but also demonstrate the relevance of specific variables in the classification process with Landsat data.

While our results using the MDI approach are promising, further studies are necessary to determine the responses of the MDI to other land features. What we presented here was an improvement in the discrimination between sparse vegetation and barren land classes by exploiting the capability of the MD to detect shape changes of the reflectance curve. It may also be worth looking at the effectiveness of the MDI for mapping when the PWR is varied or less Landsat OLI bands are used.

For the next step of this research, we will examine the possibility of applying MDI to hyperspectral images and improve the vegetation mapping at the species level. In this era of spaceborne sensors

such as the EO-1 Hyperion [96] and NASA's Hyperspectral InfraRed Imager (HypIRI) [97] that may be launched in the future, vegetation studies can be conducted with optimal use of the spectrum and using wavelengths not sampled by any broadband system [98]. Unlike broadband sensors such as the Landsat that have few bands, both spaceborne sensors have many spectral channels that span from the visible to NIR—regions considered as essential for vegetation studies. As stated by Salas and Henebry [38], MDI is applicable for the full spectrum or subsets of it. Future work will include analyzing wavelength subsets from hyperspectral datasets and how these band subsets could classify plant species. Hopefully, we could also look at the temporal changes of vegetation cover in Tajikistan using texture and MDI variables to these hyperspectral images.

Acknowledgments: This research was funded by Safari Club International Foundation (SCIF) Central Asia Program. Additional financial assistance was provided by the New Mexico State University, Agricultural Experiment Station. We are especially grateful to Joe Hosmer and Matthew Eckert for their support and encouragement. The authors are also thankful to Prof. Geoffrey Henebry of South Dakota State University for the earlier edits of the MDI Section.

Author Contributions: Eric Ariel L. Salas prepared the datasets, preprocessed the satellite image, and drafted the manuscript. Kenneth G. Boykin and Raul Valdez conceived the study and participated in the discussion of the analysis and results in great measure. Raul Valdez also collected the field summer data in the Pamir Mountains, Tajikistan.

Conflicts of Interest: The authors declare no conflict of interest.

References

1. Blaschke, T. Object-based contextual image classification built on image segmentation. In Proceedings of the 2003 IEEE Workshop on Advances in Techniques for Analysis of Remotely Sensed Data, Greenbelt, MD, USA, 27–28 October 2003; pp. 113–119.
2. Blaschke, T. Object based image analysis for remote sensing. *ISPRS J. Photogramm. Remote Sens.* **2010**, *65*, 2–16. [CrossRef]
3. Manavalan, P.; Sathyanath, P.; Rajegowda, G.L. Digital image analysis techniques to estimate waterspread for capacity evaluations of reservoirs. *Photogramm. Eng. Remote Sens.* **1993**, *59*, 1389–1395.
4. Brady, A.; Shaikh, M.; King, A.; Sharma, P. Remote sensing and the Great Cumbung Swamp. *Wetl. Aust.* **1999**, *7*, 596–606.
5. Nath, R.K.; Deb, S.K. Water-body area extraction from high resolution satellite images—An introduction, review, and comparison. *Int. J. Image Process.* **2010**, *3*, 353–372.
6. Forster, B. Some urban measurements from Landsat data. *Photogramm. Eng. Remote Sens.* **1983**, *49*, 1293–1707.
7. Shalaby, A.; Tateishi, R. Remote sensing and GIS for mapping and monitoring land cover and land-use changes in the Northwestern coastal zone of Egypt. *Appl. Geogr.* **2007**, *27*, 28–41. [CrossRef]
8. Bhaskaran, S.; Paramananda, S.; Ramnarayan, M. Per-pixel and object-oriented classification methods for mapping urban features using Ikonos satellite data. *Appl. Geogr.* **2010**, *30*, 650–665. [CrossRef]
9. Dymond, C.C.; Mladenoff, D.J.; Radeloff, V.C. Phenological differences in Tasseled Cap indices improve deciduous forest classification. *Remote Sens. Environ.* **2002**, *80*, 460–472. [CrossRef]
10. Mehner, H.; Cutler, M.; Fairbairn, D.; Thompson, G. Remote sensing of upland vegetation: The potential of high spatial resolution satellite sensors. *Glob. Ecol. Biogeogr.* **2004**, *13*, 359–369. [CrossRef]
11. Gong, P.; Howarth, P. Performance analyses of probabilistic relaxation methods for land-cover classification. *Remote Sens. Environ.* **1989**, *30*, 33–42. [CrossRef]
12. Csathó, B.; Schenk, T.; Lee, D.C.; Filin, S. Inclusion of multispectral data into object recognition. *Int. Arch. Photogramm. Remote Sens. Spat. Inf. Sci.* **1999**, *32*, 53–61.
13. Wang, Z.; Wei, W.; Zhao, S.; Chen, X. Object-oriented classification and application in land use classification using SPOT-5 PAN imagery. In Proceedings of the IEEE International, Geoscience and Remote Sensing Symposium, IGARSS '04, Anchorage, AK, USA, 20–24 September 2004; pp. 3158–3160.
14. Blundell, J.S.; Opitz, D.W. Object recognition and feature extraction from imagery: The Feature Analyst approach. *Int. Arch. Photogramm. Remote Sens. Spat. Inf. Sci.* **2006**, *36*, C42.
15. Heumann, B.W. An object-based classification of mangroves using a hybrid decision tree—Support Vector machine approach. *Remote Sens.* **2011**, *3*, 2440–2460. [CrossRef]

16. Myint, S.W.; Gober, P.; Brazel, A.; Grossman-Clarke, S.; Weng, Q. Per-pixel *vs.* object-based classification of urban land cover extraction using high spatial resolution imagery. *Remote Sens. Environ.* **2011**, *115*, 1145–1161. [[CrossRef](#)]
17. Li, C.; Wang, J.; Wang, L.; Hu, L.; Gong, P. Comparison of classification algorithms and training sample sizes in urban land classification with Landsat thematic mapper imagery. *Remote Sens.* **2014**, *6*, 964–983. [[CrossRef](#)]
18. Son, N.T.; Chen, C.F.; Chang, N.B.; Chen, C.R.; Chang, L.Y.; Thanh, B.X. Mangrove mapping and change detection in Ca Mau Peninsula, Vietnam, using Landsat data and object-based image analysis. *IEEE J. Sel. Top. Appl. Earth Obs. Remote Sens.* **2015**, *8*, 503–510. [[CrossRef](#)]
19. Blaschke, T.; Strobl, J. What's wrong with pixels? Some recent developments interfacing remote sensing and GIS. *GeoBIT/GIS* **2001**, *14*, 12–17.
20. Franklin, S.E.; Wulder, M.A.; Gerylo, G.R. Texture analysis of IKONOS panchromatic data for Douglas-fir forest age class separability in British Columbia. *Int. J. Remote Sens.* **2001**, *22*, 2627–2632. [[CrossRef](#)]
21. Zhang, J.; Li, P.; Wang, J. Urban built-up area extraction from Landsat TM/ETM+ images using spectral information and multivariate texture. *Remote Sens.* **2014**, *6*, 7339–7359. [[CrossRef](#)]
22. Coburn, C.A.; Roberts, A.C.B. A multiscale texture analysis procedure for improved forest stand classification. *Int. J. Remote Sens.* **2004**, *25*, 4287–4308. [[CrossRef](#)]
23. Agüera, F.; Aguilar, F.J.; Aguilar, M.A. Using texture analysis to improve per-pixel classification of very high resolution images for mapping plastic greenhouses. *ISPRS J. Photogramm. Remote Sens.* **2008**, *63*, 635–646. [[CrossRef](#)]
24. Arcidiacono, C.; Porto, S.M.C.; Cascone, G. Accuracy of crop-shelter thematic maps: A case study of maps obtained by spectral and textural classification of high-resolution satellite images. *J. Food Agric. Environ.* **2012**, *10*, 1071–1074.
25. Wood, E.M.; Pidgeon, A.M.; Radeloff, V.C.; Keuler, N.S. Image texture as a remotely sensed measure of vegetation structure. *Remote Sens. Environ.* **2012**, *121*, 516–526. [[CrossRef](#)]
26. St-Louis, V.; Pidgeon, A.M.; Clayton, M.K.; Locke, B.A.; Bash, D.; Radeloff, V.C. Satellite image texture and a vegetation index predict avian biodiversity in the Chihuahuan Desert of New Mexico. *Ecography* **2009**, *32*, 468–480. [[CrossRef](#)]
27. St-Louis, V.; Pidgeon, A.M.; Radeloff, V.C.; Hawbaker, T.J.; Clayton, M.K. High-resolution image texture as a predictor of bird species richness. *Remote Sens. Environ.* **2006**, *105*, 299–312. [[CrossRef](#)]
28. Rodriguez-Galiano, V.F.; Chica-Olmo, M.; Abarca-Hernandez, F.; Atkinson, P.M.; Jeganathan, C. Random Forest classification of Mediterranean land cover using multi-seasonal imagery and multi-seasonal texture. *Remote Sens. Environ.* **2012**, *121*, 93–107. [[CrossRef](#)]
29. Ciocca, G.; Corchs, S.; Gasparini, F. Complexity Perception of Texture Images. In *New Trends in Image Analysis and Processing—ICIAP 2015 Workshops*; Murino, V., Puppo, E., Sona, D., Cristani, M., Sansone, C., Eds.; Springer International Publishing: New York, NY, USA, 2015; pp. 119–126.
30. Stefanov, W.L.; Ramsey, M.S.; Christensen, P.R. Monitoring urban land cover change: An expert system approach to land cover classification of semiarid to arid urban centers. *Remote Sens. Environ.* **2001**, *77*, 173–185. [[CrossRef](#)]
31. Pesaresi, M.; Gerhardinger, A.; Kayitakire, F. A robust built-up area presence index by anisotropic rotation-invariant textural measure. *IEEE J. Sel. Top. Appl. Earth Obs. Remote Sens.* **2008**, *1*, 180–192. [[CrossRef](#)]
32. Pesaresi, M.; Gerhardinger, A. Improved textural built-up presence index for automatic recognition of human settlements in arid regions with scattered vegetation. *IEEE J. Sel. Top. Appl. Earth Obs. Remote Sens.* **2011**, *4*, 16–26. [[CrossRef](#)]
33. Wentz, E.A.; Stefanov, W.L.; Gries, C.; Hope, D. Land use and land cover mapping from diverse data sources for an arid urban environments. *Comput. Environ. Urban Syst.* **2006**, *30*, 320–346. [[CrossRef](#)]
34. Gao, T.; Zhu, J.; Zheng, X.; Shang, G.; Huang, L.; Wu, S. Mapping spatial distribution of larch plantations from multi-seasonal Landsat-8 OLI imagery and multi-scale textures using Random Forests. *Remote Sens.* **2015**, *7*, 1702–1720. [[CrossRef](#)]
35. Wang, J.; Li, C.; Hu, L.; Zhao, Y.; Huang, H.; Gong, P. Seasonal land cover dynamics in Beijing derived from Landsat 8 data using a spatio-temporal contextual approach. *Remote Sens.* **2015**, *7*, 865–881. [[CrossRef](#)]
36. Stumpf, A.; Kerle, N. Object-oriented mapping of landslides using Random Forests. *Remote Sens. Environ.* **2011**, *115*, 2564–2577. [[CrossRef](#)]

37. Salas, E.A.L.; Henebry, G.M. Separability of maize and soybean in the spectral regions of chlorophyll and carotenoids using the Moment Distance Index. *Isr. J. Plant Sci.* **2012**, *60*, 65–76. [[CrossRef](#)]
38. Salas, E.A.L.; Henebry, G.M. A new approach for the analysis of hyperspectral data: Theory and sensitivity analysis of the Moment Distance Method. *Remote Sens.* **2014**, *6*, 20–41. [[CrossRef](#)]
39. Bellman, R. *Dynamic Programming*, 2nd ed.; Dover Publications: Mineola, NY, USA, 2003.
40. Breiman, L. Bagging predictors. *Mach. Learn.* **1996**, *24*, 123–140. [[CrossRef](#)]
41. Lawrence, R.L.; Wood, S.D.; Sheley, R.L. Mapping invasive plants using hyperspectral imagery and Breiman Cutler classifications (randomForest). *Remote Sens. Environ.* **2006**, *100*, 356–362. [[CrossRef](#)]
42. Yin, P.; Criminisi, A.; Winn, J.; Essa, I. Tree-based classifiers for bilayer video segmentation. In Proceedings of the IEEE Conference on Computer Vision and Pattern Recognition, CVPR'07, Minneapolis, MN, USA, 17–22 June 2007; pp. 1–8.
43. Salas, E.A.L.; Valdez, R.; Boykin, K.G. Geographic layers as landscape drivers for the Marco Polo Argali habitat in the southeastern Pamir Mountains of Tajikistan. *ISPRS Int. J. Geo-Inf.* **2015**, *4*, 2094–2108. [[CrossRef](#)]
44. Valdez, R.; Michel, S.; Subbotin, A.; Klich, D. Status and population structure of a hunted population of Marco Polo Argali *Ovis ammon polii* (Cetartiodactyla, Bovidae) in Southeastern Tajikistan. *Mammalia* **2015**. [[CrossRef](#)]
45. Vanselow, K.A.; Kraudzun, T.; Samimi, C. Land stewardship in practice: An example from the eastern Pamirs of Tajikistan. In *Rangeland Stewardship in Central Asia*; Squires, V., Ed.; Springer: Dordrecht, The Netherlands, 2012; pp. 71–90.
46. Breckle, S.W.; Wucherer, W. 16 Vegetation of the Pamir (Tajikistan): Land use and desertification problems. In *Land Use Change and Mountain Biodiversity*; Spehn, E., Liberman, M., Körner, C., Eds.; Taylor & Francis: Boca Raton, FL, USA, 2006; pp. 225–237.
47. Breu, T.; Maselli, D.; Hurni, H. Knowledge for sustainable development in the Tajik Pamir Mountains. *Mt. Res. Dev.* **2005**, *25*, 139–146. [[CrossRef](#)]
48. PALM. *Strategy and Action Plan for Sustainable Land Management in the High Pamir and Pamir-Alai Mountains*; 2011.
49. Hergarten, C. *Investigations on Land Cover and Land use of Gorno Badakhshan (GBAO) by Means of Land Cover Classifications Derived from LANDSAT 7 Data Making Use of Remote Sensing and GIS Techniques*; University of Bern: Bern, Switzerland, 2004.
50. U.S. Geological Survey Earth Resources Observation and Science (USGS EROS) Resource Archive. Available online: <http://eros.usgs.gov/> (accessed on 20 July 2015).
51. Walter, H.; Breckle, S. *Spezielle Ökologie der Gemäßigten und Arktischen Zonen Euro-Nordasiens*; Fischer: Stuttgart, Germany, 1986.
52. Giri, C.; Muhlhausen, J. Mangrove forest distributions and dynamics in Madagascar (1975–2005). *Sensors* **2008**, *8*, 2104–2117. [[CrossRef](#)]
53. Zandler, H.; Brenning, A.; Samimi, C. Quantifying dwarf shrub biomass in an arid environment: Comparing empirical methods in a high dimensional setting. *Remote Sens. Environ.* **2015**, *158*, 140–155. [[CrossRef](#)]
54. Lu, D.; Weng, Q. Urban classification using full spectral information of Landsat ETM+ imagery in Marion County, Indiana. *Photogramm. Eng. Remote Sens.* **2005**, *71*, 1275–1284. [[CrossRef](#)]
55. Chavez, P.S. An improved dark-object subtraction technique for atmospheric scattering correction of multispectral data. *Remote Sens. Environ.* **1988**, *24*, 459–479. [[CrossRef](#)]
56. Mather, P.; Koch, M. *Computer Processing of Remotely-Sensed Images: An Introduction*; John Wiley & Sons: Hoboken, NJ, USA, 2011.
57. Guyot, G.; Gu, X.F. Effect of radiometric corrections on NDVI-determined from SPOT-HRV and Landsat-TM data. *Remote Sens. Environ.* **1994**, *49*, 169–180. [[CrossRef](#)]
58. Hall, D.K.; Riggs, G.A.; Salomonson, V.V. Development of methods for mapping global snow cover using moderate resolution imaging spectroradiometer data. *Remote Sens. Environ.* **1995**, *54*, 127–140. [[CrossRef](#)]
59. Vanselow, K.A.; Samimi, C. Predictive mapping of dwarf shrub vegetation in an arid high mountain ecosystem using remote sensing and random forests. *Remote Sens.* **2014**, *6*, 6709–6726. [[CrossRef](#)]
60. Palacio-Prieto, J.L.; Luna-Gonzalez, L. Improving spectral results in a GTS context. *Int. J. Remote Sens.* **1996**, *17*, 2201–2209. [[CrossRef](#)]

61. Strahler, A.H.; Logan, T.L.; Bryant, N.A. Improving forest cover classification accuracy from Landsat by incorporating topographic information. In Proceedings of the 12th International Symposium on Remote Sensing of the Environment, Manila, Philippines, 20–26 April 1978.
62. Janssen, L.F.; Jaarsma, J.; van der Linder, E. Integrating topographic data with remote sensing for land-cover classification. *Photogramm. Eng. Remote Sens.* **1990**, *56*, 1503–1506.
63. U.S. Geological Survey Shuttle Radar Topography Mission (SRTM) Resource Archive. Available online: <http://srtm.usgs.gov/index.php> (accessed on 20 July 2015).
64. Qi, J.; Chehbouni, A.; Huete, A.R.; Kerr, Y.H.; Sorooshian, S. A modified soil adjusted vegetation index. *Remote Sens. Environ.* **1994**, *48*, 119–126. [[CrossRef](#)]
65. Chehbouni, A.; Kerr, Y.H.; Qi, J.; Huete, A.R.; Sorooshian, S. Toward the development of a multidirectional vegetation index. *Water Resour. Res.* **1994**, *30*, 1281–1286. [[CrossRef](#)]
66. Pickup, G.; Chewings, V.H.; Nelson, D.J. Estimating changes in vegetation cover over time in arid rangelands using landsat MSS data. *Remote Sens. Environ.* **1993**, *43*, 243–263. [[CrossRef](#)]
67. Richardson, A.J.; Weigand, C.L. Distinguishing vegetation from soil background information. *Photogramm. Eng. Remote Sens.* **1977**, *43*, 1541–1552.
68. Rajesh, K.; Jawahar, C.V.; Sengupta, S.; Sinha, S. Performance analysis of textural features for characterization and classification of SAR images. *Int. J. Remote Sens.* **2001**, *22*, 1555–1569. [[CrossRef](#)]
69. Culbert, P.D.; Pidgeon, A.M.; St-Louis, V.; Bash, D.; Radeloff, V.C. The impact of phenological variation on texture measures of remotely sensed imagery. *IEEE J. Sel. Top. Appl. Earth Obs. Remote Sens.* **2009**, *2*, 299–309. [[CrossRef](#)]
70. Haralick, R.M.; Shanmugam, K.; Dinstein, I. Textural features for image classification. *IEEE Trans. Syst. Man Cybern.* **1973**, *SMC-3*, 610–621. [[CrossRef](#)]
71. Pacifici, F.; Chini, M.; Emery, W.J. A neural network approach using multi-scale textural metrics from very high-resolution panchromatic imagery for urban land-use classification. *Remote Sens. Environ.* **2009**, *113*, 1276–1292. [[CrossRef](#)]
72. Kimothi, M.M.; Dasari, A. Methodology to map the spread of an invasive plant (*Lantana camara* L.) in forest ecosystems using Indian remote sensing satellite data. *Int. J. Remote Sens.* **2010**, *31*, 3273–3289. [[CrossRef](#)]
73. Zhang, X.; Feng, X.; Jiang, H. Object-oriented method for urban vegetation mapping using IKONOS imagery. *Int. J. Remote Sens.* **2010**, *31*, 177–196. [[CrossRef](#)]
74. ENVI Guide. *Programmer's Guide*; ITT Visual Information Solutions: Boulder, CO, USA, 2009.
75. Frohn, R.C.; Autrey, B.C.; Lane, C.R.; Reif, M. Segmentation and object-oriented classification of wetlands in a karst Florida landscape using multi-season Landsat-7 ETM+ imagery. *Int. J. Remote Sens.* **2011**, *32*, 1471–1489. [[CrossRef](#)]
76. Gilead, U. *Locating and Examining Potential Sites for Vicarious Radiometric Calibration of Space Multi-Spectral Imaging Sensors in the Negev Desert*; Ben-Gurion University of the Negev: Beersheba, Israel, 2005.
77. Staben, G. Mapping the Spatial and Temporal Distribution of *Melaleuca* spp. on the Magela Floodplain between 1950 & 2004 Using Object-Based Analysis and GIS. Bachelor's Thesis, Charles Darwin University, Darwin, NT, USA, June 2008.
78. Tiner, R.W.; Lang, M.W.; Klemas, V.V. *Remote Sensing of Wetlands: Applications and Advances*; CRC Press: Boca Raton, FL, USA, 2015.
79. Homer, C.; Dewitz, J.; Fry, J.; Coan, M.; Hossain, N.; Larson, C.; Herold, N.; McKerrow, A.; VanDriel, J.N.; Wickham, J. Completion of the 2001 national land cover database for the conterminous United States. *Photogramm. Eng. Remote Sens.* **2007**, *73*, 337–341.
80. Li, F.; Clausi, D.A.; Wong, A. Comparative study of classification methods for surficial materials in the Umiujalik Lake region using RADARSAT-2 polarimetric, Landsat-7 imagery and DEM data. *Can. J. Remote Sens.* **2015**, *41*, 29–39. [[CrossRef](#)]
81. Waske, B.; van der Linden, S.; Oldenburg, C.; Jakimow, B.; Rabe, A.; Hostert, P. Imagerf—A user-oriented implementation for remote sensing image analysis with Random Forests. *Environ. Model. Softw.* **2012**, *35*, 192–193. [[CrossRef](#)]
82. Duro, D.C.; Franklin, S.E.; Dubé, M.G. Multi-scale object-based image analysis and feature selection of multi-sensor earth observation imagery using random forests. *Int. J. Remote Sens.* **2012**, *33*, 4502–4526. [[CrossRef](#)]

83. Congalton, R.; Mead, R. A quantitative method to test for consistency and correctness in photointerpretation. *Photogramm. Eng. Remote Sens.* **1983**, *49*, 69–74.
84. Jensen, J.R. *Introductory Digital Image Processing*, 3rd ed.; Prentice-Hall: Upper Saddle, NJ, USA, 2005.
85. Fuller, R.M.; Smith, G.M.; Devereux, B.J. The characterisation and measurement of land cover change through remote sensing: Problems in operational applications? *Int. J. Appl. Earth Obs. Geoinf.* **2003**, *4*, 243–253. [[CrossRef](#)]
86. Yuan, F.; Sawaya, K.E.; Loeffelholz, B.C.; Bauer, M.E. Land cover classification and change analysis of the Twin Cities (Minnesota) Metropolitan Area by multitemporal Landsat remote sensing. *Remote Sens. Environ.* **2005**, *98*, 317–328. [[CrossRef](#)]
87. Anderson, J.R. *A Land Use and Land Cover Classification System for Use with Remote Sensor Data*; U.S. Government Printing Office: Washington, DC, USA, 1976.
88. Mallinis, G.; Emmanoloudis, D.; Giannakopoulos, V.; Maris, F.; Koutsias, N. Mapping and interpreting historical land cover/land use changes in a Natura 2000 site using earth observational data: The case of Nestos delta, Greece. *Appl. Geogr.* **2011**, *31*, 312–320. [[CrossRef](#)]
89. Maillard, P. Comparing texture analysis methods through classification. *Photogramm. Eng. Remote Sens.* **2003**, *69*, 357–367. [[CrossRef](#)]
90. Laliberte, A.S.; Fredrickson, E.L.; Rango, A. Combining decision trees with hierarchical object-oriented image analysis for mapping arid rangelands. *Photogramm. Eng. Remote Sens.* **2007**, *73*, 197–207. [[CrossRef](#)]
91. Eiumnoh, A.; Shrestha, R.P. Application of DEM data to Landsat image classification: Evaluation in a tropical wet-dry landscape of Thailand. *Photogramm. Eng. Remote Sens.* **2000**, *66*, 297–304.
92. Huete, A.R.; Hua, G.; Qi, J.; Chehbouni, A.; van Leeuwen, W.J.D. Normalization of multidirectional red and NIR reflectances with the SAVI. *Remote Sens. Environ.* **1992**, *41*, 143–154. [[CrossRef](#)]
93. USGS. What Are the Best Spectral Bands to Use for My Study? Available online: http://landsat.usgs.gov/best_spectral_bands_to_use.php (accessed on 15 October 2015).
94. Kraudzun, T.; Vanselow, K.A.; Samimi, C. Realities and myths of the Teresken Syndrome—An evaluation of the exploitation of dwarf shrub resources in the Eastern Pamirs of Tajikistan. *J. Environ. Manag.* **2014**, *132*, 49–59. [[CrossRef](#)] [[PubMed](#)]
95. Liu, D.; Xia, F. Assessing object-based classification: Advantages and limitations. *Remote Sens. Lett.* **2010**, *1*, 187–194. [[CrossRef](#)]
96. Pearlman, J.S.; Barry, P.S.; Segal, C.C.; Shepanski, J.; Beiso, D.; Carman, S.L. Hyperion, a space-based imaging spectrometer. *IEEE Trans. Geosci. Remote Sens.* **2003**, *41*, 1160–1173. [[CrossRef](#)]
97. Mariotto, I.; Thenkabail, P.S.; Huete, A.; Slonecker, E.T.; Platonov, A. Hyperspectral versus multispectral crop-productivity modeling and type discrimination for the HypSPIRI mission. *Remote Sens. Environ.* **2013**, *139*, 291–305. [[CrossRef](#)]
98. Roberts, D.A.; Roth, K.L.; Perroy, R.L. Hyperspectral remote sensing of vegetation. In *Hyperspectral Vegetation Indices*; CRC Press: Boca Raton, FL, USA, 2012; pp. 309–328.



© 2016 by the authors; licensee MDPI, Basel, Switzerland. This article is an open access article distributed under the terms and conditions of the Creative Commons by Attribution (CC-BY) license (<http://creativecommons.org/licenses/by/4.0/>).